# Portable Doppler/FSK/FMCW Radar Systems for Life Activity Sensing and Human Localization

Changzhi Li, Jing Wang, Daniel Rodriguez, Ashish Mishra, Zhengyu Peng, and Yiran Li

***Abstract*—This paper presents recent progress on portable Doppler, frequency-shift keying (FSK) and frequency-modulated continuous-wave (FMCW) radar systems for life activity sensing and human localization. It starts from a software-based calibration technology that significantly improves the accuracy and reliability of millimeter-wave interferometry radar front-end for physiological motion and vocal vibration detection. Then, the operation principle and unique features of FSK and FMCW radar, such as RF/digital beamforming, for human-aware sensing and localization will be presented. To reject clutter noise, which is a common challenge for practical deployment of short-range radar system, intermodulation radar technique will be discussed. Then, machine learning will be presented as an efficient approach to make the radar system smart for automatic classification and decision making. Finally, challenges for biomedical radar systems and future development directions will be discussed.**

*Keywords*—**Biomedical Radar, Doppler, FSK, FMCW, multiple-input multiple-output, Millimeter-wave, Beamforming.**

## I. Introduction

Portable biomedical radar systems with embedded control and signal processing have the potential to improve the quality of life in many healthcare, human-computer interface, and internet of things (IoT) applications.

Coherent short-range radars operating in interferometry mode are very sensitive to small motions and thus have been extensively investigated for vital signs monitoring by measuring physiological motions [1][2] and auditory analysis by detecting vocal folds vibrations [3][4]. Since the phase-based detection benefits from a shorter wavelength for larger motion-induced phase shift, the carrier frequencies have been moved from lower industrial, scientific and medical (ISM) radio bands such as 2.4/5.8 GHz to 24 GHz, and further into millimeter-wave (mm-wave) range such as 60 GHz and beyond [5]. On the other hand, continuous-wave (CW) radars can detect micro-Doppler induced by limb motion, and thus have been used in applications such as gesture and gait monitoring, with the help of advanced machine learning algorithms [6]. By modulating the radio frequency carrier signal with schemes such as frequency-shift keying (FSK) or linear frequency-modulation, modern portable radars can also obtain the absolute range information of targets. This ranging capability offered by frequency modulation combined with the physiological activity sensing enabled by coherent phase detection leads to human-aware tracking [7]. Furthermore, electronic control of the radar radiation beam pattern enables angular scanning of the space, thus makes it possible for biomedical radar to carry out human-centered two-dimension (2D) or even three-dimension (3D) mapping tasks. To suppress clutter noise in a typical complex living environment, nonlinear sensing technologies including harmonic/sub-harmonic radar and intermodulation radar are also developed [8]-[10]. All these functionalities are made possible on a low-power portable platform because of the recent advancement in semiconductor technologies, embedded signal processing, and sophisticated real-time algorithms.

This paper presents the authors' recent research activities in smart microwave radar sensors aided with advanced technologies including digital/RF beamforming and machine learning. Several radar systems operating in interferometry, Doppler, frequency-modulated continuous-wave (FMCW), and FSK modes at 5.8 GHz, 24 GHz, and 120 GHz will be discussed. These systems can potentially benefit biomedical and healthcare applications such as sleep study [11][12] and fall detection [13]-[15]. Case studies will be presented on human-aware indoor localization and anomaly detection.

The paper is organized as follows. Section II discusses Doppler and interferometry radars that operate up to 125 GHz with sub-micrometer sensitivity for physiological and vocal motion sensing. Section III discusses FSK radar, which switches between two carrier frequencies that carry out Doppler/interferometry detection, for human tracking. Section IV discusses FMCW radar aided with digital/RF beamforming for human-aware imaging and tracking. Section V presents non-linear radar techniques, with a focus on intermodulation radar, for clutter rejection in complex environments. Section VI uses anomaly detection as a case study to illustrate the advantage of machine learning for microwave radar systems. Finally, a conclusion and future works of the group will be presented in Section VI.

## II. Millimeter-wave Doppler/Interferometry Radar

Due to its high sensitivity, mm-wave Doppler/interferometry radars have become a very popular topic within the microwave community. Nevertheless, challenges such as in-phase/quadrature ($I/Q$) phase/amplitude imbalance, dc offset, and the undesired harmonics due to

C. Li, J. Wang, D. Rodriguez, A. Mishra, Z. Peng, and Y. Li are with the Electrical and Computer Engineering Department, Texas Tech University, Lubbock, TX 79409, USA (e-mail: changzhi.li@ttu.edu).

978-1-7281-0878-0/19/$31.00 ©2019 IEEE

large-angle phase modulation for short wavelengths must be overcome before it could be widely adopted [16].

Many solutions have been proposed to avoid the previously described distortions in order to maintain the signal integrity. For instance, several analog compensation circuits to correct the imbalance of reference signals from the local oscillator (LO) have been proposed [17]. Moreover, in order to overcome the dc offset, dc-coupled receivers have been proposed, avoiding the distortion induced by the ac-coupling circuits [18][19]. Another promising solution to overcome the dc offset and phase imbalances is the use high-speed digitizer in order to sample the intermediate frequency (IF). It was shown in [20] and [21] that this method can effectively offset the imbalances for speech information sensing. However, the previously discussed solutions add hardware complexity and increase the cost of the system. Although, blind digital estimation methods were proposed in [22]-[24] for phase/amplitude imbalance correction to avoid the use of complex hardware, they induce a high computational load due to its high complexity for interferometry applications.

For vital signs detection, the desired heartbeat signal can be overwhelmed by the undesired harmonics due to the respiration and random body movement large-angle phase modulation for short wavelengths [25]. This undesirable effect becomes even worse in mm-wave receivers since any small movement could be comparable or even bigger than λ.

To illustrate the undesired effects discussed above, experiments were carried out in lab environment using an ac-coupled 125 GHz interferometric radar based on the Silicon Radar TRX_120_001 on-chip frontend. In the experiments, a laptop was used to digitalize the signal with a sampling frequency of 40 Hz and 14-bit resolution. The subjects are two healthy males of 1.9 and 1.72 meter height. Their weight was measured as 100 and 70 kg respectively. During the experiments, the subjects were seated 1 m away from the radar, one at a time, and they were asked to breathe normally.

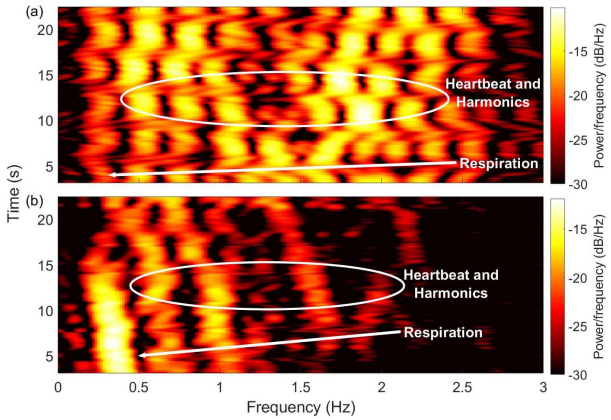


Fig. 1. Respiration and heartbeat spectrogram: (a) 1.9 m and 100 kg subject, (b) 1.72 m and 70 kg subject.

Fig. 1 presents the spectrogram of the recorded time-domain signal by the 125-GHz radar. As can be seen, the heartbeat signals are indistinguishable from the generated harmonics making their detection impossible. From Fig. 1, it can also be seen that due to the subject's different physical features they generate a very particular harmonic signature, for instance the biggest subject generated higher number of harmonics. Although this is an undesired effect for vital signs detection, it could be very useful for applications such as a biological password, gender discrimination, and physical features detection.

To overcome the harmonics undesired effect, the advantages of arctangent demodulation (ATD) were demonstrated in [26]. However, it was also shown that ATD is sensitive to dc offset and *I*/*Q* channels imbalances. In the other hand, complex signal demodulation (CSD) is immune to dc offset but it can be affected by the undesired harmonics. Therefore, a digital distortion correction technique for a 125-GHz radar was proposed and tested in [16]. The proposed distortion correction method proved to be very effective restoring the signal balance to offset the distortion and recover the ideal *I*/*Q* constellation.

### *A. Physiological and Vocal Motion Sensing*

The effects of signal distortion in ATD and CSD for speech detection have been already discussed in [20] and [26]. Therefore, to validate the effectiveness of the distortion correction method proposed by the authors in [16], the ac-coupled 125-GHz radar was used for physiological and vocal motion sensing. In the experiments, a laptop was used to digitalize the signal with a sampling frequency of 32000 Hz and 16-bit resolution. A cell phone was used to record a reference signal through its embedded microphone. The subject is a healthy male without phonation disorders. During the experiment, the subject was asked to remain seated, with the throat exposed to the radar at a distance of 50 cm. During the experiment several background noise sources such as the ventilation fans close to the outlets in the ceiling were present. The subject was asked to speak in English "The sky is blue". In a normal tone. Nobody else was speaking during the experiment.

Fig. 2 presents the recorded time-domain signal by the 125-GHz radar and its *I*/*Q* constellation. As can be seen, the signal is distorted by the random body movement and the *I*/*Q* channel imbalances. To mitigate the random body movement, which is more notorious in mm-wave radar systems, a high-pass filter with a 100-Hz cutoff frequency was used to process the recovered signals.

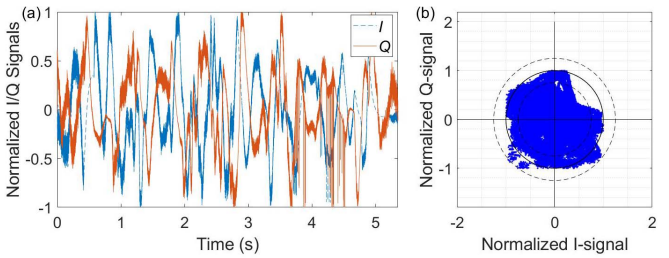


Fig. 2. Radar-detected signals: (a) Normalized *I*/*Q*, (b) Normalized *I*/*Q* constellation.

The spectrograms of the radar-demodulated and microphone-detected signals are shown in Fig. 3. As shown in Fig. 3(a), the CSD result is shifted and some noise is present in the signal, which entails to a low correlation with the microphone-detected signal shown in Fig. 3(c). In contrast, for the ATD spectrogram in Fig. 3(b), there is not a defined

spectrogram and the noise predominates in the signal. However, these results were expected since ATD is more sensitive to channel imbalances than CSD.

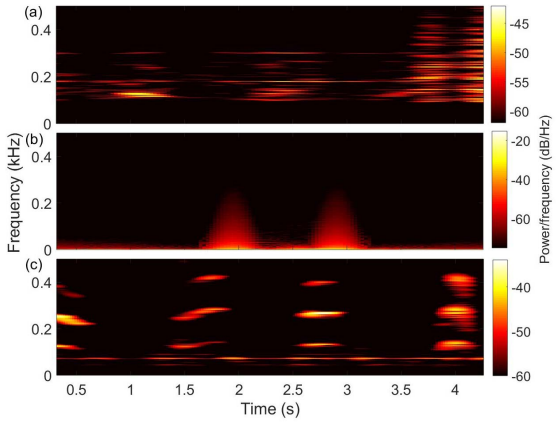


Fig. 3. Spectrograms of: (a) CSD applied to radar-detected signals, (b) ATD applied to radar-detected signals, (c) Microphone-detected signal.

To improve the obtained results, the distortion correction method proposed by the authors was applied to the radar-recovered signals. It is shown in Fig. 4 that the proposed method can overcome the *I*/*Q* channels imbalances and recover the *I*/*Q* constellation. From Fig. 4(b), the total phase shift applied to the signal by the throat was calculated as approximately 8° which corresponds to 55 μm motion. Additionally, the spectrogram of the corrected signals was calculated and compared with the microphone-detected signal as shown in Fig. 5. Comparing the two figures, the radar-detected result correlates well with the microphone-detected one, verifying the effectiveness of the proposed method.

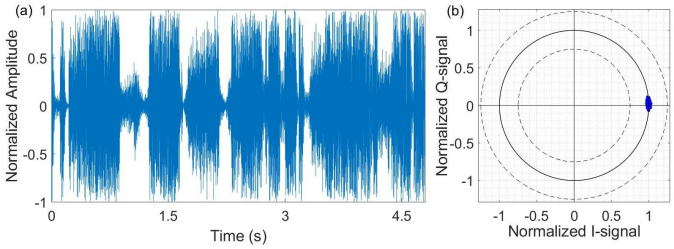


Fig. 4. Radar-detected signals with distortion correction: (a) Normalized baseband signal, (b) Normalized *I*/*Q* constellation.

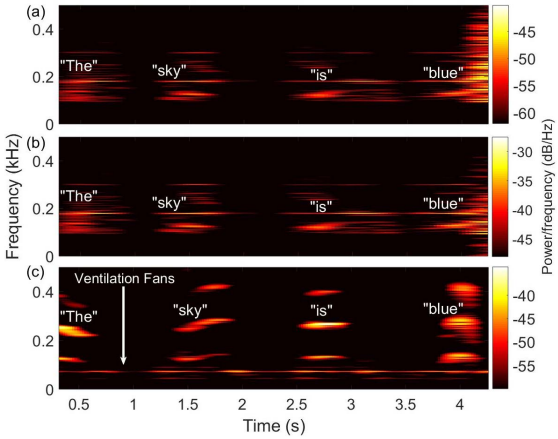


Fig. 5. Improved spectrograms of: (a) CSD applied to radar-detected signals, (b) ATD applied to radar-detected signals, (c) Microphone-detected signal.

## III. FSK Radar for Moving and Stationary Human Detection

In an FSK radar system, two carrier frequencies $f_1$ and $f_2$ are switched back and forth in time domain, which is illustrated in Fig. 6. The frequency shift between the two carriers is usually very small compared with the carrier frequencies, i.e., in the kHz or MHz range, which is represented as $\Delta f = f_2 - f_1$, assuming $f_2 > f_1$. Due to the switching mechanism, two discrete responses associated with the two transmit signals exist in each baseband channel. It should be noted that the switching frequency should be sufficiently fast so that all motion information is well sampled in spite of the switching modulation. The phase offset between the carrier responses introduced by the switching mechanism needs to be compensated if the carrier responses are to be processed directly, which is discussed in [27].

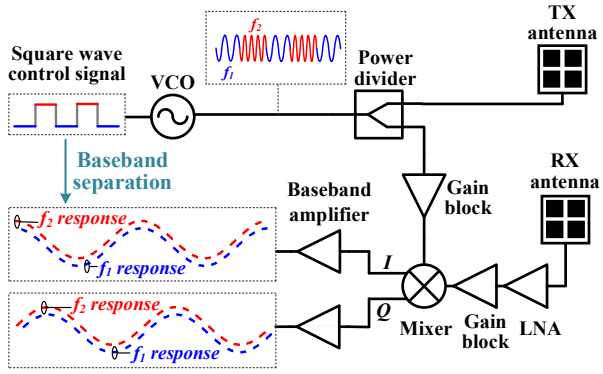


Fig. 6. Block diagram of the 5.8 GHz FSK radar system.

### A. Range Tracking of Moving Human Subject

Range tracking of moving target and vital sign monitoring using FSK radar have been demonstrated in [28]. For range tracking of moving human target, the received signals will be shifted in frequency due to the Doppler effect, producing baseband responses that contain the Doppler frequencies generated by the moving target, expressed as $f_{d,k} = 2vf_k/c$, where $f_{d,k}$ stands for the Doppler frequency, $c$ is the speed of light, $v$ is the speed of the target, and $f_k$ represents the carrier frequency, $k = 1, 2$. By keeping $\Delta f$ very small in comparison with $f_k$, $f_{d,1}$ and $f_{d,2}$ will be almost identical, i.e., $f_{d,1} \approx f_{d,2}$. However, due to this small frequency shift between the carriers, baseband responses will separate along with the travel distance of the radar signals, as illustrated in Fig. 7. Since phase difference is proportional to the round-trip travel distance of the signal, the distance measurement can be derived as $R = c\Delta\varphi/(4\pi\Delta f)$, where $\Delta\varphi$ is the phase difference between the two baseband responses. Because $\Delta\varphi$ can only reach a maximum of $2\pi$, the maximum unambiguous range is limited, which can be obtained accordingly as $R_{max} = c/(2\Delta f)$. Nonetheless, for a given application, the frequency shift can be adjusted to meet the detection range requirement. The maximum unambiguous range can also be extended by utilizing more than two carriers [29] or modulating at least one of the carriers. If high measurement resolution and long range coverage are both demanded, other reference system

can be adopted to extend the maximum discernible range without sacrificing the measurement resolution [30].

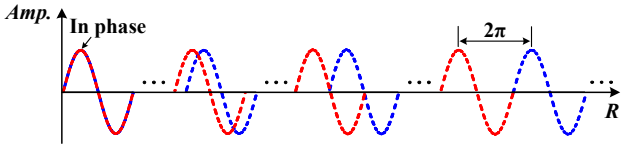


Fig. 7. FSK radar baseband responses with respect to distance for moving human tracking.

In the implemented 5.8-GHz FSK radar system, a 400-Hz square wave signal is generated on board, which is used as the control signal of the free-running voltage-controlled oscillator (VCO). The two carrier frequencies are 5.83 GHz and 5.84 GHz with a frequency shift of 10 MHz, resulting in a maximum unambiguous range of 15 m. An example using the 5.8-GHz FSK radar for single moving subject tracking is given in Fig. 8, where a human subject completed two round trips from 2 m to 12 m with a normal walking speed in an interior corridor. Both the square wave and *I/Q* channels were recorded using NI USB-6009 with 10 kHz sampling frequency. The square wave control signal was utilized to separate the baseband responses for carrier tones $f_1$ and $f_2$. Fast Fourier transform (FFT) was applied on the complex baseband signal with 0.085-s FFT window length, hamming window, and zero-padding. By comparing the phase difference between the obtained Doppler frequencies on both frequency spectra, the instantaneous range of the walking subject was estimated according to the previous FSK range equation.

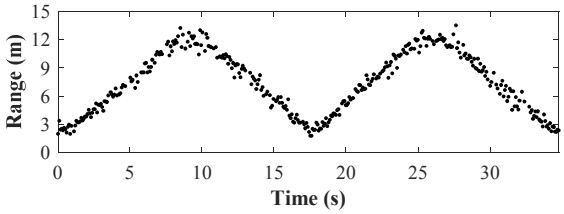


Fig. 8. Range tracking result of a single subject walking back and forth.

Multiple subjects tracking experiment was carried out with two human subjects walking in opposite directions in the same environment. One subject walked from 2 m to 12 m while the other subject walked from 12 m to 2 m. Both subjects started and stopped the movement around the same time with a normal walking speed. The same FFT settings as in the single subject tracking experiment were used. After applying FFT on the carrier responses, the Doppler frequency peaks associated with the two subjects were successfully separated in the frequency domain and the phase extraction was realized separately on the associated Doppler peaks. Fig. 9 plots the range tracking results. It was observed that due to multipath interference, the obtained Doppler peaks associated with the two carriers are not always identical to each other. The more the Doppler peaks vary, the larger the range error becomes. Therefore, in the measurement, only the Doppler peak pairs that were within 1.8 Hz frequency difference were kept to effectively remove the distorted Doppler frequencies.

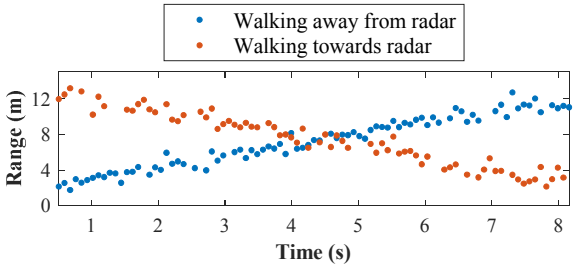


Fig. 9. Range tracking result of two subjects walking in opposite directions.

### *B. Range Detection of Stationary Human Subject*

The localization capability of stationary human subject was further extended in [31] based on the phase information extracted from the detected vital sign signals. When the target of interest has a periodic small motion $x(t) = m\cdot\sin\omega_0 t$ at a nominal distance $D_0$, where $m$ stands for the motion peak amplitude and $\omega_0$ represents the motion frequency, the radar signal will be reflected back with its phase modulated by the time-varying periodic motion and a constant phase determined by $D_0$. Different from the linear motion scenario, the acquired baseband signal will be frequency-modulated by the periodic motion frequency, which can be represented using spectral analysis [32] as:

$$B_k(t) = \exp\left[j\left(\frac{4\pi x(t)}{\lambda_k} + \frac{4\pi D_0}{\lambda_k} + \varphi_k\right)\right] = \sum_{n=-\infty}^{\infty} \mathrm{J}_n\left(\frac{4\pi m}{\lambda_k}\right)\exp\left[j\left(n\omega_0 t + \frac{4\pi D_0}{\lambda_k} + \varphi_k\right)\right], \quad (1)$$

where $\mathrm{J}_n$ is the $n$-th order Bessel function of the first kind. The baseband signal is represented by the sum of a series of sinusoids at harmonic frequencies of the motion frequency with their amplitudes determined by the corresponding Bessel function and a constant phase determined by the nominal distance. Note that the phase difference of any $n$-th order frequency pair is consistent, which is:

$$\Delta\varphi(t) = \frac{4\pi D_0}{\lambda_2} - \frac{4\pi D_0}{\lambda_1}. \quad (2)$$

Accordingly, the target range can be estimated as $D_0 = c\Delta\varphi/(4\pi\Delta f)$. Therefore, the phase difference extraction is not restricted to a specific frequency pair on the spectra. To achieve reliable range estimation, the strongest harmonic pairs should be selected due to the corresponding highest signal-to-noise ratio (SNR) when compared to the rest of the frequency pairs. In addition, if the noise is additive white Gaussian noise, its components will be distributed across the spectrum. The noise influence is almost negligible on the frequency peaks on the spectrum. Compared with the *I/Q* trajectory based phase acquisition method [31], [33], phase extraction at the strongest frequency pairs enhances SNR and enables robust nominal distance estimation.

Considering that the tiny physiological motions are more prone to multipath interference than the large walking motions, a 24-GHz FSK radar (InnoSent IVS-162) equipped with two 4 × 2 patch antennas was used for range detection of stationary human subject due to its narrower antenna beam width than the 5.8-GHz FSK radar that has 2 × 2 patch

antennas. A 700-Hz square wave control frequency is generated by an external board, which switches the transmit frequency between 23.8279 GHz and 23.8306 GHz with a frequency shift of 2.7 MHz. The maximum unambiguous range is calculated as 55.5 m.

Stationary human subject detection experiments were conducted with the 24-GHz FSK radar in the same interior corridor. Photograph of the experimental setup is shown in Fig. 10(a). A seated human subject breathed normally during the measurement time period of 60 s. Three measurements were performed when the subject was 1 m, 1.5 m, and 2 m from the radar, respectively. Fig. 10(b) shows a segment of the recorded *I* channel data when the subject was at 1.5 m. The correspondence between the square wave amplitude levels and the carrier responses is demonstrated in the zoom-in view. The corresponding spectra are presented in Fig. 10(c). By comparing the phase difference between the detected respiration tones on both spectra, the absolute range of the subject was estimated. A 25-s FFT sliding window was used with a 5-s step size. Eight range estimations were obtained for each measurement. The average range error was calculated as the difference between the average of the eight range estimations and the ground truth. The average error and standard deviation results for the three measurements are listed in Table I.

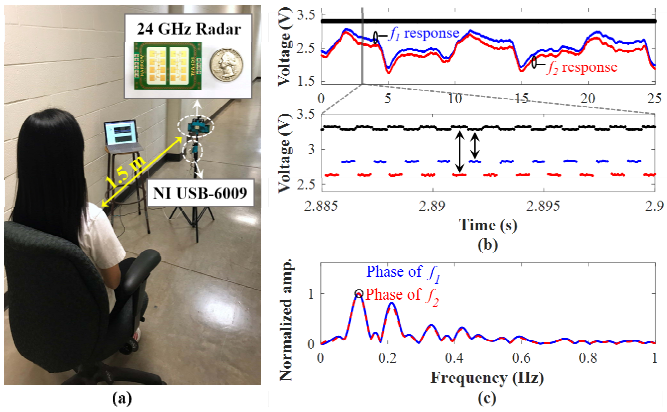


Fig. 10. (a) Range detection setup of a seated human subject at 1.5 m in an interior corridor. (b) A segment of the recorded *I* channel respiration signal and square wave control signal at 1.5 m. (c) Corresponding spectra of (b).

TABLE I
AVERAGE RANGE ERROR/STANDARD DEVIATION RESULTS OF A SEATED HUMAN SUBJECT AT THREE LOCATIONS.

| Ground truth | 1 m | 1.5 m | 2 m |
|---|---|---|---|
| **Average range error** / standard deviation (m) | **0.07** / 0.06 | **-0.07** / 0.10 | **-0.14** / 0.20 |
| | **0.10** / 0.07 | **-0.11** / 0.12 | **-0.33** / 0.09 |
| | **-0.02** / 0.13 | **-0.18** / 0.04 | **0** / 0.17 |

It can be seen that 77.8% of the range error were within ±10% of the ground truth, with the largest error being -0.33 m at 2 m, corresponding to -16.5% of the ground truth and -0.6% of the maximum unambiguous range. Extensive experimentation has revealed that multipath interference is likely the main contribution to the range fluctuation among other possible error sources including frequency drift [34], *I*/*Q* channel mismatch [35], [36], effect of antenna directivity, and measurement error. Nevertheless, the results have demonstrated acceptable accuracy of using FSK technology for range detection of stationary human subjects based on the vital signs.

## IV. FMCW RADAR WITH DIGITAL/RF BEAMFORMING

FMCW radar transmits a linear modulated chirp signal to targets. The reflected signal has a time delay, which corresponds to the time of the electromagnetic wave travelling round-trip from the radar to the target. The reflected signal is processed by the radar receiver and mixed with a replica of the transmitted chirp signal. A baseband beat signal, whose frequencies are directly correspondence to the range of the targets, are obtained. FFT can be applied to the baseband beat signal to obtain the range information of targets. With multiple chirps and coherence processing, Doppler information relating to the motion properties of targets can also be obtained with range-Doppler processing by applying FFT along a series of range profiles [37], [38].

An FMCW radar can perform a 2D scan of 3D scene with digital or RF beamforming, while the third dimension can be measured from the radar beat signals. For an array of antennas, the radiation patterns can be controlled by changing the phase and amplitude of the signal in each antenna channel. The phase and amplitude control can be performed either in the RF domain or in the digital baseband domain, which is referred to as RF beamforming or digital beamforming, respectively.

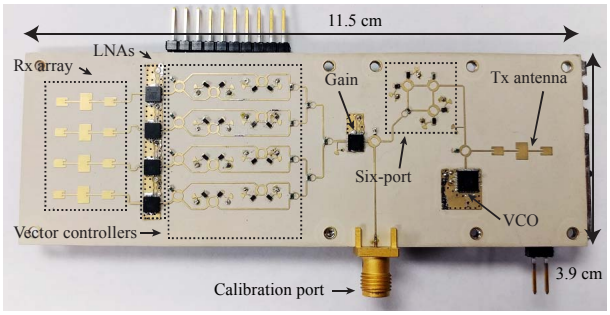


Fig. 11. Photos of the proposed radar prototype. From [44].

For RF beamforming, phased array is used. Conventionally, a dedicated phase shifter is required for each antenna channel to control the phase of the RF signal. However, the high cost of phase shifters results in a high system cost. In recent decades, novel RF beamforming techniques emerged for applications at higher frequencies [39]-[42]. One of the promising solutions is vector modulator [43], [44]. A vector modulator divides the RF signal into an *I* and a *Q* signal. The amplitudes of *I* and *Q* signals are controlled separately by a pair of variable gain amplifiers (VGA) or attenuators. Then, these two signals are added together. A vector modulator can simultaneously control the phase and amplitude of an RF signal. In [44], a *K*-band portable FMCW radar with RF beamforming array was reported. Fig. 11 is the photo of the RF beamforming radar prototype. This prototype includes both the transmitter and the receiver. The transmitter utilizes a free-running VCO, which is controlled by a "sawtooth" voltage to synthesize chirp signal. The operating frequency covers 23.5 GHz to 24 GHz. A patch antenna is used to

transmit chirp signals. On the receiver side, there is a four-channel array antenna connected to an array of vector modulators. The vector modulators are realized with simple microwave structures and low-cost diodes. A six-port circuit is used to de-ramp the chirp signal. The main beam of the receiver array can be continuously steered with a range from -45° to 45°. The audio card of a laptop is used to sample the beat signal from the radar receiver. A 2D localization experiment has been performed with a car, a lamppost and a human subject in the field of view of the radar prototype. The experimental environment is shown in Fig. 12. Fig. 13 illustrates the experiment results, where signatures of the car, the lamppost and the human subject are clearly seen. In addition, by extracting the vital-Doppler signals, the human signature can be isolated from other targets, as shown in Fig. 14.


Fig. 12. Experimental environment of short-range localization with a human subject and two object targets using the proposed radar prototype. From [44].

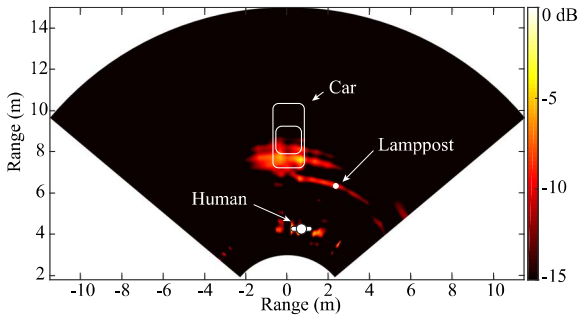


Fig. 13. Measured result of the short-range localization experiment with a human subject and two object targets using the proposed radar prototype. From [44].

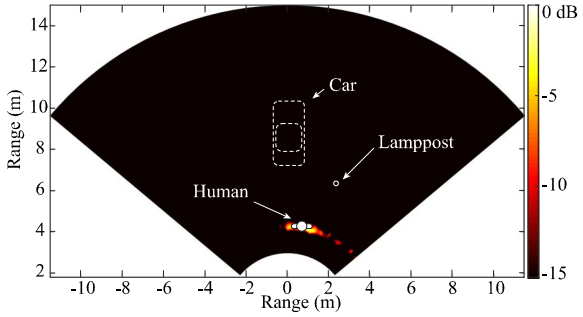


Fig. 14. Human target extracted with standard deviation of 10 sequencing scans. From [44].

It is known that a digital beamforming system provides high phase and amplitude accuracy compared with an RF beamforming system. However, it usually requires high-speed analog-to-digital converters (ADCs) or digital-to-analog converters (DACs) for all the antenna channels. Due to the massive use of high-speed mixed signal devices, the cost and power consumption of a digital beamforming system are usually high. In [45], a non-uniformly spaced sparse array combined with time division multiplexing (TDM) multiple-input multiple-output (MIMO) FMCW radar system was designed and built at 24 GHz. The sparse array used in the design can effectively increase the angular resolution of the radar by increasing the effective aperture. Randomness in the antenna spacing is introduced in the array to eliminate the grating lobes. Moreover, the MIMO technique used in the designed radar system synthesizes a larger planar array with a relatively small number of antenna elements.

The photograph of the radar RF board is shown in Fig. 15. The array contains 16 transmitter elements and 16 receiver elements. The synthesized virtual array is a 16×16 non-uniformly spaced planar array. For the transmitter, two K-band phase-locked loops (PLLs) are used to synthesize the chirp signals. Customized K-band RF switches are used to extend the four-channel transmitters to 16 channels. On the receiver side, four four-channel radar receiver chips are used to process the received chirp signal. The baseband signals from these receiver chips are processed by baseband amplifiers and sampled by an ADC on a Wi-Fi board by TDM. The sampled baseband data is transmitted to a computer for post-processing through Wi-Fi.

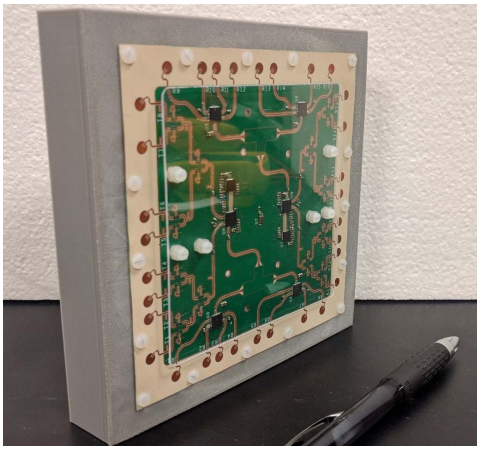

Fig. 15. Photo of the RF board of the K-band 3D MIMO radar prototype.

The engineered MIMO radar prototype has been used for a 3D short range localization experiment. The photo of the experiment environment is shown in Fig. 16(a). In the experiment, the radar was fixed on the back of a car and powered by the car battery. Half of the system, i.e., 8×8 non-uniformly spaced planar array was used. There were three corner reflectors with different ranges and heights in radar's field of view. It took 0.64 s to complete a single scan to generate 64-channel beat signals. Fig. 16(b) illustrates the 3D localization result of the experiment. The detected ranges of the three corner reflectors are at 1.6 m, 2.3 m, and 3.14 m, respectively. The correct heights and azimuth angles are also obtained. For comparison, it needs a 12×12 planar array for a phased array to achieve the same performance. With a

conventional MIMO radar not using a non-uniformly spaced array, it requires at least 12 transmitters and 12 receivers.

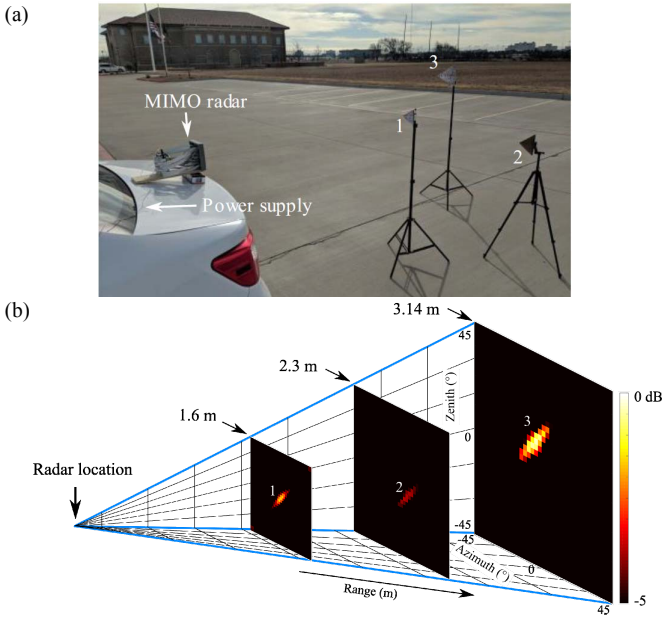


Fig. 16. (a) Photo of the experiment setup. (b) 3D images of the three targets with the MIMO radar prototype. From [45].

## V. Intermodulation Radar for Clutter Rejection

CW radars working on fundamental frequencies can track small displacements [46]. But their performance is affected by clutter motion in the background and can be overwhelmed if the clutter motion is very large compared to the motion of the point of interest.

To solve this issue, active backscatter-based radars were developed utilizing an active tag with an oscillator that modulates the reflected frequency by $f \pm f_m$, where $f$ is the fundamental tone of the radar and $f_m$ is the modulated frequency generated by the oscillator in the tag. Another commonly used radar is subharmonic radar [47]. The frequency divider in the tag divides the frequency by a factor of $n$, which could be any number greater than 2. The divided frequency tone is sent back towards the radar receiver. These two types of radars need an active power supply for their operation. Therefore, their operation is limited by the battery life and involves expensive components. Another category used for clutter suppression is harmonic radars [8]. One of their key advantages is that they can work with passive tags without any power supply, making the life span of tag dependent on wear and tear of tag only. However, harmonic radars operate across different frequency bands and thus have challenge in spectrum licensing and design complexity.

In this section, an intermodulation radar is discussed, which works on the principle of third-order intermodulation (IM3). The system has advantages over the three radar systems discussed above, such as (1) licensing issue as all the transmitted and reflected frequencies lie in the same band; (2) unlike harmonic responses that suffer from 6 dB more pathloss compared with fundamental, intermodulation responses have the same pathloss as fundamental tones; (3) unlike harmonic tags that need matching for both fundamental and harmonic bands, the design of passive tag for intermodulation radar is simple as matching need to be considered in one frequency band only; (4) unlike the prior three radars that need two antennas or dual-band antennas, single-frequency antenna is sufficient for intermodulation radar [9].

This example considers two frequency tones, $f_1$ at 5.79 GHz and $f_2$ at 5.84 GHz, for an intermodulation radar. The tag is made of flexible substrate making it easy to wear. Fig. 17 shows the block diagram of the radar. Two experiments were conducted to demonstrate the clutter rejection. The third experiment was conducted to show the vital signs measurement conducted by the radar.

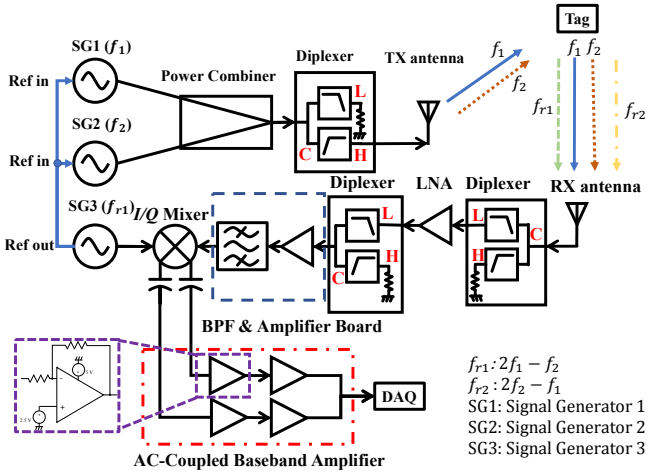


Fig. 17. Intermodulation radar.

### A. Experiment 1: Mechanical motion discrimination

In this experiment, the radar was set up to measure clutter and tag motion. A copperplate was used as the clutter. The radar cross section (RCS) of the tag was around 12.9 m$^2$ while clutter had a maximum RCS of 22.7 m$^2$. Here clutter was approximately twice as large as the tag. The measurements were done at 1 m distance between the tag/clutter and the radar. The motion amplitude was set at 1 mm peak-to-peak and frequency of motion was 0.9 Hz for both the tag and the clutter.

The baseband signal was recorded with a sampling frequency of 20 Hz by NI-USB 6009. Fig. 18 shows the spectrum of the baseband signal. It is shown that the tag had a prominent peak at 0.9 Hz while the clutter reflection was below the noise floor. Hence, radar was able to successfully discriminate between the clutter and the target motions even though the clutter had a larger RCS than the tag.

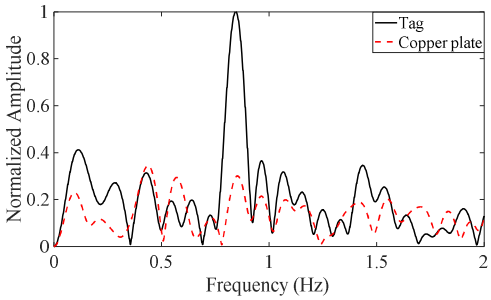


Fig. 18. Baseband spectrum for mechanical motion measurement.

### B. Experiment 2: Measurement with a large clutter

With the radar operating in interferometry mode, the breathing pattern of a human subject (P1) was recorded. One person (P2) acting as a large clutter was asked to move in a predefined path of 1.5m behind P1. It took P2 approximately 2 seconds to complete the movement. The speed of P2 was around 0.75 m/s. Based on velocity to Doppler frequency conversion, this motion may affect the FFT spectrum at around 28 Hz.

Fig. 19 shows the measured spectrum, where only vital signs peaks are present. There is no peak around 28 Hz. This shows that the radar was successful in supressing the interference due to clutter. This measurement was recorded with the human subject sitting around 1 m from radar. It is shown that this radar can be used to measure the vital signs of the human subjects in a real-world scenario with moving clutters of similar sizes.

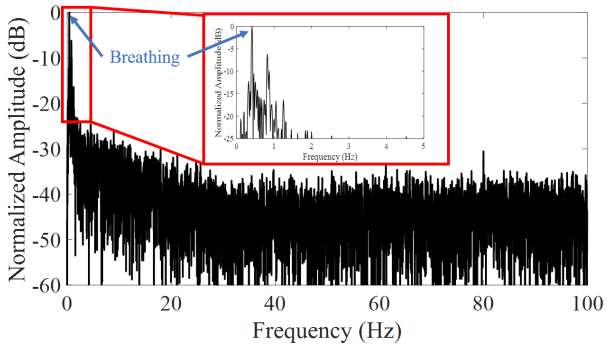


Fig. 19. Spectrum of breathing measurement with a large clutter.

### C. Experiment 3: Vital signs measurement

The radar was used to measure the vital signs of a human target. The tag was placed on the back of P1 and aligned with the subject's heart to capture the weak displacement signal due to heartbeat. P1 was asked to sit in front of the radar with the back facing the radar. FFT and short-time Fourier transform (STFT) was performed on the captured signal. Fig. 20(a) shows the baseband data obtained by the intermodulation radar. The corresponding spectrum was plotted and shown in Fig. 20(b). Fig. 20(c) shows the STFT of the data. For STFT, Kaiser window of 15-second size was used and the step size was 0.5 seconds. The measurement was performed at 0.5 m distance away from the radar.

## VI. Machine Learning for Modern Radar Systems

Machine learning is widely used in modern radar systems for classification purposes. In this section, an example of detecting a potential active shooter with concealed rifle/shotgun is presented. A custom-designed portable 5.8-GHz hybrid-mode FMCW-Doppler radar sensor [38] is used in this study. The identification is based on radar micro-Doppler and range-Doppler signatures analysis. Special features are extracted from micro-Doppler and range-Doppler signatures of human subjects carrying a concealed rifle and other seven similar activities. Artificial neural network (ANN) is employed in this study for activity classification.

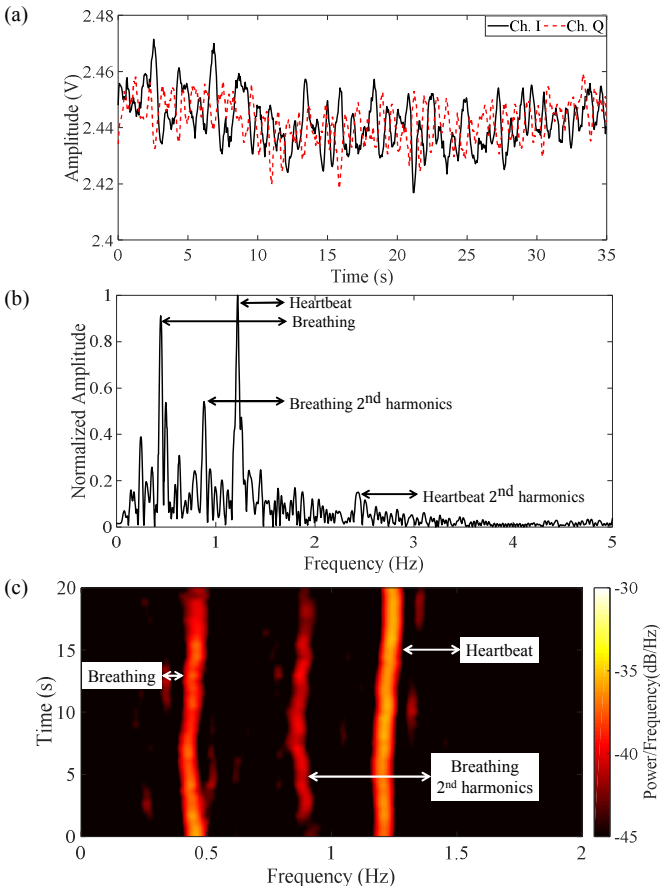


Fig. 20. Vital signs. (a) Baseband signal; (b) FFT result (c) STFT result.

### A. Micro-Doppler and Range-Doppler

Fig. 21 shows an example of micro-Doppler (a) and range-Doppler (b) signatures when a human subject walks to the radar sensor without holding anything.

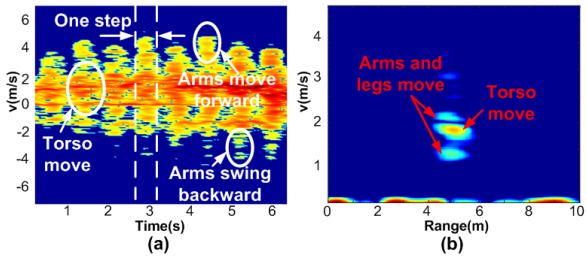


Fig. 21. An example of micro-Doppler (a) and range-Doppler (b) signatures of a human subject walks toward the radar without holding anything.

Radar micro-Doppler signature is obtained by applying STFT to the radar output when the radar works in the Doppler mode. Micro-Doppler contains different velocity information for different parts of a human body. As shown in Fig. 21(a), the human subject walks 8 steps toward the radar. The velocity of the human subject's torso is about 2 m/s while the speed of his/her arms is around 4m/s. On the micro-Doppler signature, the positive velocities are caused by the human body parts moving toward the radar while the negative velocities are caused by the parts of the human target receding from the radar.

Range-Doppler signature is obtained from the beat signal output from the radar sensor when the radar works in the

FMCW mode. It provides range and velocity information of a moving target. Fig. 21(b) is an example of a range-Doppler signature. Compared with Fig. 21(a), the torso and limbs movement can be identified on the range-Doppler. The range-Doppler also provides the absolute distance between the radar and the moving target. This information is very helpful for locating a potential active shooter.

### B. *Experiment and Results*

Experiments were carried out to demonstrate the capability of using micro-Doppler and range-Doppler signatures to identify a person walking with a concealed rifle/shotgun. In the experiment, a radar sensor was mounted on a tripod and a human subject was asked to start from seven meters away and walk toward the radar with different activities. Thirteen human subjects were used and each of them was asked to perform every activity for four times.

In the experiments, eight activities were performed by human subjects: (a) walking with a concealed rifle under trench coat, (b) walking without holding anything, (c) walking with a cane for the blind, (d) walking with a gym bag, (e) walking with a laptop, (f) walking with a walker, (g) moving in a wheelchair, and (h) walking with a rolling suitcase. Experiment results for each activity can be found in [48].

Special patterns can be found on micro-Doppler and range-Doppler signatures of each activity. For example, for the human subject walking with a concealed rifle case, the metal muzzle of the gun that traveled with the longest distance in each step produced strong reflection and led to a high power density on the micro-Doppler signature. After studying and comparing the micro-Doppler and range-Doppler from each activity, special features are discovered for identifying potential active shooter with concealed rifle.

### C. *Feature Extraction and Activity Classification*

In order to achieve high activity classification accuracy, feature extraction is very important. In this example, four features are extracted from the micro-Doppler signature and one feature is extracted from the range-Doppler signature for activity recognition. Those features are computed from the micro-Doppler and range-Doppler signatures.

Four features extracted from micro-Doppler signature are defined as [49]:

1) *Frequency gap (FG):* the gap between torso movement and the high-energy signature on micro-Doppler caused by muzzle of the rifle or the metal tip of an object;
2) *Total bandwidth (TB):* the difference between the largest positive frequency shift and the lowest negative frequency shift;
3) *Torso speed (TS)*: the speed corresponds to the highest power density point;
4) *Limb speed difference on different directions*: the absolute difference between the limb speeds on each direction.

One feature extracted from range-Doppler signature is defined as *Aspect ratio (w/l)*: the length on the velocity direction divides the length of the range direction for the selected echo.

Fig. 22 shows an example of feature extraction from micro-Doppler signature (a) and range-Doppler (b) when a human subject walks toward the radar with a concealed rifle. After extracting features from micro-Doppler and range-Doppler signatures, the ANN was adopted for activity classification [50]. The ANN inputs are the five computed features and the outputs are eight identified activities. In this example, a total of 4158 samples were collected. To test the ANN's capability, 70%, 15%, and 15% of the samples were used for training, validating, and testing, respectively. Detailed confusion matrix of the activity classification results can be found in [48]. The classification result of identifying human subjects carrying a concealed rifle from other similar activities achieved 99.21% accuracy.

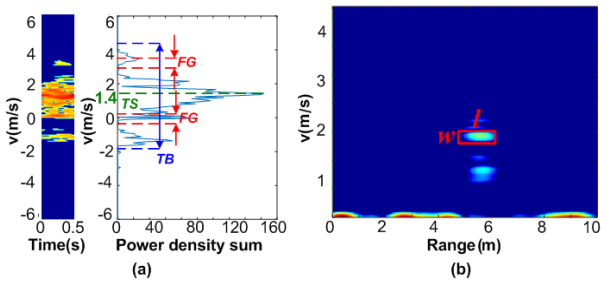


Fig. 22. Feature extraction from micro-Doppler (a) and range-Doppler (b) when a human subject walks toward the radar with a concealed rifle.

## VII. Conclusion

Biomedical radar systems can remotely detect human physiological motions and track life activities without any device attached to the body. Existing researches have opened the possibility to improve the quality of life by offering low-cost solutions for long-term vital signs monitoring, catching prodromal symptoms of cardiac diseases, warning of sudden infant death syndrome (SIDS), sleep disorder study, fall detection, human tracking, and rehabilitation assistance. While the potential of biomedical radar technology is attracting, there are still challenges to overcome. To date, most reported works have targeted on monitoring human subjects under ideal conditions, i.e., the subject was instructed to sit still or lie down in a quiet environment in the absence of other moving objects. On the one hand, a small random body motion could be comparable or even stronger than heartbeat and breathing induced physiological motion, and thus overwhelm the desired signal. On the other hand, the activities of other objects and people around the subject of interest may also create high levels of interference. Therefore, some of the future works will be focused on reliable sensing and tracking that are robust against body movement noise and environmental interference. In addition, minimization of the sensing devices into a small form factor, ideally system-on-chip, and low-power low-cost solutions will be pursued.

## Acknowledgment

The authors would like to acknowledge grant support from National Science Foundation (NSF) CNS-1718483 and ECCS-1808613.

## REFERENCES


[1] J. C. Lin, "Microwave sensing of physiological movement and volume change: A review," *Bioelectromagnetics*, vol. 13, no. 6, pp. 557-565, 1992.

[2] A. D. Droitcour, O. Boric-Lubecke, V. M. Lubecke, J. Lin, and G. T. A. Kovacs, "Range correlation and I/Q performance benefits in single-chip silicon Doppler radars for noncontact cardiopulmonary monitoring," *IEEE Trans. Microw. Theory Techn.*, vol. 52, no. 3, pp. 838-848, Mar. 2004.

[3] H. Hong, H. Zhao, Z. Peng, H. Li, C. Gu, C. Li, and X. Zhu, "Time-varying vocal folds vibration detection using a 24 GHz portable auditory radar," *Sensors*, vol. 16, no. 8, p.1181, Jul. 2016.

[4] C. Lin, S. Chang, C. Chang, and C. Lin, "Microwave human vocal vibration signal detection based on Doppler radar technology," *IEEE Trans. Microw. Theory Techn.*, vol. 58, no. 8, pp. 2299-2306, Aug. 2010.

[5] T. J. Kao, Y. Yan, T. Shen, A. Y. Chen, and J. Lin, "Design and analysis of a 60-GHz CMOS Doppler micro-radar system-in-package for vital-sign and vibration detection," *IEEE Trans. Microw. Theory Techn.*, vol. 61, no. 4, pp. 1649-1659, Apr. 2013.

[6] M. G. Amin, Y. D. Zhang, F. Ahmad, and K. C. D. Ho, "Radar signal processing for elderly fall detection: the future for in-home monitoring," *IEEE Signal Process. Mag.*, vol. 33, no. 2, pp. 71-80, Mar. 2016.

[7] G. Wang, C. Gu, T. Inoue, and C. Li, "A hybrid FMCW-interferometry radar for indoor precise positioning and versatile life activity monitoring," *IEEE Trans. Microw. Theory Techn.*, vol. 62, no. 11, pp. 2812-2822, Nov. 2014.

[8] A. Singh and V. M. Lubecke, "Respiratory monitoring and clutter rejection using a CW doppler radar with passive RF tags," *IEEE Sensors J.*, vol. 12, no. 3, pp. 558-565, Mar. 2012.

[9] A. Mishra and C. Li, "5.8-GHz ISM band intermodulation radar for high-sensitivity motion-sensing applications," *IEEE Radio and Wireless Symposium (RWS)*, Anaheim, CA, 2018, pp. 4-6.

[10] L. Chioukh, H. Boutayeb, D. Deslandes, and K. Wu, "Noise and sensitivity of harmonic radar architecture for remote sensing and detection of vital signs," *IEEE Trans. Microw. Theory Techn.*, vol. 62, no. 9, pp. 1847-1855, Sep. 2014.

[11] H. Hong *et al.*, "Microwave sensing and sleep: noncontact sleep-monitoring technology with microwave biomedical radar," *IEEE Microw. Mag.*, vol. 20, no. 8, pp. 18-29, Aug. 2019.

[12] L. Zhang, J. Xiong, H. Zhao, H. Hong, X. Zhu, and C. Li, "Sleep stages classification by CW Doppler radar using bagged trees algorithm," *2017 IEEE Radar Conference (RadarConf)*, Seattle, WA, 2017, pp. 0788-0791.

[13] C. Ding, Y. Zou, L. Sun, H. Hong, X. Zhu, and C. Li, "Fall detection with multi-domain features by a portable FMCW radar," *IEEE MTT-S International Wireless Symposium (IWS)*, Guangzhou, China, 2019, pp. 1-3.

[14] C. Garripoli, M. Mercuri, P. Karsmakers, P. J. Soh, G. Crupi, G.A. E. Vandenbosch, C. Pace, P. Leroux, and D. Schreurs, "Embedded DSP-based telehealth radar system for remote indoor fall detection," *IEEE J. Biomed. Health Inform.*, vol. 19, no. 1, pp. 92–101, Jan. 2015.

[15] Q. Wu, Y. D. Zhang, W. Tao, and M. G. Amin, "Radar-based fall detection based on Doppler time-frequency signatures for assisted living," *IET Radar, Sonar & Navigation*, vol. 9, no. 2, pp. 164–172, Feb. 2015.

[16] D. Rodriguez and C. Li, "A digital I/Q correction technique for a 125-GHz interferometric radar with sub-micrometer sensitivity," *IEEE MTT-S International Microwave Symposium (IMS)*, Boston, MA, 2019, pp. 301-304.

[17] E. Liu, J. Wang, and T. Wang, "Phase imbalance compensation in SAR/ISAR quadrature demodulation," *2nd Asian-Pacific Conference on Synthetic Aperture Radar*, Xian, Shanxi, 2009, pp. 459-463.

[18] X. Zhao, C. Song, V. Lubecke, and O. Boric-Lubecke, "DC coupled Doppler radar physiological monitor," *Annual International Conference of the IEEE Engineering in Medicine and Biology Society*, Boston, MA, 2011, pp. 1909–1912.

[19] D. Tang, J. Wang, Z. Peng, Y. Chiang, and C. Li, "A DC-coupled biomedical radar sensor with analog DC offset calibration circuit," *IEEE International Instrumentation and Measurement Technology Conference (I2MTC)*, Houston, TX, 2018, pp. 1–6.

[20] S. Li *et al.*, "A 94-GHz millimeter-wave sensor for speech signal acquisition," *Sensors (Switzerland)*, vol. 13, no. 11, pp. 4248–14260, Nov. 2013.

[21] F. Chen *et al.*, "A novel method for speech acquisition and enhancement by 94 GHz millimeter-wave sensor," *Sensors (Switzerland)*, vol. 16, no. 1, pp. 1–14, Jan. 2016.

[22] A. Singh et al., "Data-based quadrature imbalance compensation for a CW Doppler radar system," *IEEE Trans. Microw. Theory Techn.*, vol. 61, no. 4, pp. 1718-1724, Apr. 2013.

[23] M. Windisch and G. Fettweis, "Blind I/Q imbalance parameter estimation and compensation in low-IF receivers," *First International Symposium on Control, Communications and Signal Processing*, Hammamet, Tunisia, 2004, pp. 75-78.

[24] E. Cetin, I. Kale, and R. C. S. Morling, "Adaptive compensation of analog front-end I/Q mismatches in digital receivers," *ISCAS 2001. The 2001 IEEE International Symposium on Circuits and Systems (Cat. No.01CH37196)*, Sydney, NSW, 2001, vol. 4, pp. 370–373.

[25] C. Li and J. Lin, "Random body movement cancellation in doppler radar vital sign detection," *IEEE Trans. Microw. Theory Tech.*, vol. 56, no. 12, pp. 3143–3152, Dec. 2008.

[26] H. Zhao, Z. Peng, H. Hong, X. Zhu, and C. Li, "A portable 24-GHz auditory radar for non-contact speech sensing with background noise rejection and directional discrimination," *IEEE MTT-S International Microwave Symposium (IMS)*, San Francisco, CA, 2016, pp. 1-4.

[27] J. Muñoz-Ferreras, J. Wang, T. Zhou, R. Gomez-Garcia, C. Li, and L. Ran, "Accuracy improvement in range measurements of short-range FSK radars," *IEEE MTT-S International Wireless Symposium (IWS)*, Chengdu, 2018, pp. 1-4.

[28] J. Wang and C. Li, "A human tracking and physiological monitoring FSK technology for single senior at home care," *40th Annual International Conference of the IEEE Engineering in Medicine and Biology Society (EMBC)*, Honolulu, HI, 2018, pp. 4432-4435.

[29] H. Zhang and K. Wu, "Three-frequency principle for automotive radar system," *Proc. IEEE Radio and Wireless Conference*, Atlanta, GA, 2004, pp. 315-318.

[30] J. Wang, Z. Peng, and C. Li, "An efficient and extended range tracking method using a hybrid FSK-FMCW system," *IEEE MTT-S International Wireless Symposium (IMS)*, Chengdu, 2018, pp. 1-4.

[31] J. Wang, T. Karp, J. M. Muñoz-Ferreras, R. Gómez-García, and C. Li, "A spectrum-efficient FSK radar solution for stationary human subject localization based on vital sign signals," *IEEE MTT-S International Microwave Symposium (IMS)*, Boston, MA, USA, 2019, pp. 140-143.

[32] C. Li, Y. Xiao, and J. Lin, "Experiment and spectral analysis of a low-power Ka-band heartbeat detector measuring from four sides of a human body," *IEEE Trans. Microw. Theory Techn.*, vol. 54, no. 12, pp. 4464-4471, Dec. 2006.

[33] C. Gu and J. Lien, "A two-tone radar sensor for concurrent detection of absolute distance and relative movement for gesture sensing," *IEEE Sensors Lett.*, vol. 1, no. 3, pp. 1-4, Jun. 2017.

[34] F. Ahmad, M. G. Amin, and P. D. Zemany, "Dual-frequency radars for target localization in urban sensing," *IEEE Trans. Aerosp. Electron. Syst.*, vol. 45, no. 4, pp. 1598-1609, Oct. 2009.

[35] F. Ahmad, M. G. Amin, and P. D. Zemany, "Performance analysis of dual-frequency CW radars for motion detection and ranging in urban sensing applications," *Proc. SPIE Symposium on Defense and Security*, Orlando, FL, Apr. 2007.

[36] Y. Yan, C. Li and J. Lin, "Effects of I/Q mismatch on measurement of periodic movement using a Doppler radar sensor," *IEEE Radio and Wireless Symposium (RWS)*, New Orleans, LA, 2010, pp. 196-199.

[37] Z. Peng and C. Li, "Portable Microwave Radar Systems for Short-Range Localization and Life Tracking: A Review," *Sensors (Switzerland)*, vol. 19, no. 5, p. 1136, Mar. 2019.

[38] Z. Peng et al., "A portable FMCW interferometry radar with programmable low-IF architecture for localization, ISAR imaging, and vital sign tracking," *IEEE Trans. Microw. Theory Tech.*, vol. 65, no. 4, pp. 1334–1344, Dec. 2017.

[39] M. S. Lee and Y. H. Kim, "Design and performance of a 24-GHz switch-antenna array FMCW radar system for automotive applications," *IEEE Trans. Veh. Technol.*, vol. 59, no. 5, pp. 2290-2297, Jun. 2010.

[40] W. Lee, J. Kim, and Y. J. Yoon, "Compact two-layer rotman lens-fed microstrip antenna array at 24 GHz," *IEEE Trans. Antennas Propag.*, vol. 59, no. 2, pp. 460-466, Feb. 2011

[41] M. Morinaga, T. Nagasaku, H. Shinoda, and H. Kondoh, "24GHz intruder detection radar with beam-switched area coverage," *IEEE MTT-S International Microwave Symposium (IMS)*, Honolulu, HI, Jun. 2007, pp. 389-392.
[42] H. Jia, L. Kuang, W. Zhu, Z. Wang, F. Ma, Z. Wang, and B. Chi, "A 77 GHz frequency doubling two-path phased-array FMCW transceiver for automotive radar," *IEEE J. Solid-State Circuits*, vol. 51, no. 10, pp. 2299-2311, Oct. 2016.
[43] T. Yu and G. M. Rebeiz, "A 22-24 GHz 4-element CMOS phased array with on-chip coupling characterization," *IEEE J. Solid-State Circuits*, vol. 43, no. 9, pp. 2134-2143, Sep. 2008
[44] Z. Peng, L. Ran, and C. Li, "A *K*-band portable FMCW radar with beamforming array for short-range localization and vital-Doppler targets discrimination," *IEEE Trans. Microw. Theory Tech.*, vol. 65, no. 9, pp. 3443–3452, Sep. 2017.
[45] Z. Peng and C. Li, "A portable *K*-band 3-D MIMO radar with nonuniformly spaced array for short-range localization," *IEEE Trans. Microw. Theory Tech.*, vol. 66, no. 11, pp. 5075-5086, Nov. 2018.
[46] T. J. Kao, Y. Yan, T. Shen, A. Y. Chen, and J. Lin, "Design and analysis of a 60-GHz CMOS Doppler micro-radar system-in-package for vital-sign and vibration detection," *IEEE Trans. Microw. Theory Tech.*, vol. 61, no. 4, pp. 1649-1659, Apr. 2013.
[47] N. El Agroudy, M. El-Shennawy, N. Joram, and F. Ellinger, "Design of a 24 GHz FMCW radar system based on sub-harmonic generation" *IET Radar, Sonar & Navigation*, vol. 12, no. 9, pp. 1052-1057, Sep. 2018.
[48] Y. Li, Z. Peng, R. Pal, and C. Li, "Potential active shooter detection based on radar micro-Doppler and range-Doppler analysis using artificial neural network," *IEEE Sensor J.*, vol. 19, no. 3, pp. 1052-1063, Feb. 2019.
[49] Y. Kim and H. Ling, "Human activity classification based on micro-Doppler signatures using a support vector machine," *IEEE Trans. Geosci. Remote Sensing*, vol. 47, no. 5, pp. 1328-1337, May 2009.
[50] Y. Kim and H. Ling, "Human activity classification based on micro-Doppler signature using an artificial neural network," *IEEE Antennas and Propagation Society International Symposium*, San Diego, CA, 2008, pp. 1-4.